Desalination and Water Treatment
www.deswater.com

doi: 10.5004/dwt.2020.25265

191 (2020) 29–39
July

Effect of design and operating parameters on power generation in reverse electrodialysis (RED): experimental analysis and modeling

Jaehyun Ju[a], Yongjun Choi[a], Sangho Lee[a,*], Hanki Kim[b], Namjo Jung[b]

[a]*School of Civil and Environmental Engineering, Kookmin University, Jeongneung-Dong, Seongbuk-Gu, Seoul, Korea, Tel. +82-02-910-5060; Fax: +82-02-910-8597; email: sanghlee@kookmin.ac.kr (S. Lee)*
[b]*Jeju Global Research Center, Korea Institute of Energy Research, 200 Haemajihaean-ro, Gujwa-eup, Jeju, Korea*

Received 23 August 2019; Accepted 29 November 2019

ABSTRACT

This paper investigated the effect of key parameters such as the number of cell pairs, flow rate, temperature, and salt concentration on the power output characteristics of a reverse electrodialysis (RED) system. Experiments were carried out to measure the open-circuit voltage (OCV) and maximum power (P_{max}) in a bench-scale RED system. The Nernst–Plank flux equations, together with the Donnan equilibrium relations and the electrical neutrality condition, were used to interpret experiments values. Results showed that the OCV and P_{max} increased with an increase in the number of cell pairs and temperature. Using 20 cell pairs, the OCV and P_{max} were 2.75 V and 1.4 W/m^2, respectively. The flow rate affected the OCV and P_{max} but also led to an increase in the pressure drop in the RED stack. Thus, the flow rate was suggested to be 60 mL/min with the use of 20 cell pairs in our system. The OCV and P_{max} were higher at a higher salinity difference between the high salinity and low salinity solutions. Nevertheless, the OCV and P_{max} were smaller at a higher salt concentration even if the salinity gradient between the high and low salinity solutions were the same.

Keywords: Salinity gradient power (SGP); Reverse electrodialysis (RED); Open circuit voltage (OCV); Power density; Model validation

1. Introduction

Increasing concerns about the depletion of fossil fuels and environmental issues have led to the necessity for sustainable energy production from renewable sources [1,2]. Technologies for harvesting renewable energy such as solar, wind, and geothermal sources have attracted great attention and have developed extensively recently [3]. Recently, salinity gradient power (SGP) has sparked global interest due to its high potential as a renewable energy source [3–6]. SGP is the energy extracted upon the mixing of waters with different salt concentrations [4]. In theory, 0.70–0.75 kWh (2.5–2.7 MJ) is dissipated when 1 m^3 of river water mixes with 1 m^3 of seawater [7]. Accordingly, the global potential of SGP corresponds to about 1.9 TW, which is estimated from the amount of water mixing in the world's estuaries [8].

There are several approaches to exploit SGP, including pressure retarded osmosis (PRO) and reverse electrodialysis (RED) [5]. PRO process converts osmotic pressure into mechanical energy [3,9] and an additional step is required to covert the osmotic power to electricity [10]. On the other hand, the RED process directly turns osmotic power into electricity and does not require additional conversion [11]. Accordingly, RED is more appropriate than PRO if the generation of electricity from SGP is required. RED uses a stack of alternating cation exchange membranes (CEMs) and anion exchange membranes (AEMs), in which the chemical potential difference between high salinity and low salinity water generates a voltage over the membranes [8]. This allows the direct generation of electricity from the salinity gradient [12,13]. Although there are pros and cons in PRO and RED technologies [3], the focus of this paper is the RED

* Corresponding author.

Presented at the 12th International Desalination Workshop (IDW2019), 28–30 August 2019, Jeju, Korea

technology due to its ability to generate electricity without additional steps.

In RED, a CEM that selectively permeates only cations and an AEM that selectively permeates only anions are stacked in the RED device [14–18]. If there are high and low salinity fluids flowing between the CEM and the AEM, ions move through these membranes [13,19], which generate a potential inside the stack [12,13]. In the RED module component, spacers are placed between the ion exchange membranes [13,20,21]. The efficiency of the RED system largely relies on the performance of the ion exchange membranes [22,23]. Nevertheless, other design and operating factors also significantly affect overall efficiency [24,25].

Up to now, RED technology has evolved by the development of RED membranes and spacers, optimization of operational conditions, and development of hybrid processes [26]. There have been many studies on electrodes, electrode solutions, and performance prediction models [13,23,25,27,28]. Nevertheless, RED has not been demonstrated in full-scales due to its relatively high cost and technological uncertainties. Only three pilot plants based on RED technology have been constructed and operated: the first one is in Afsluitdijk, the Netherlands, by the company RED stack B.V., and the second one is in Marsala, Italy, within the European project REA Power, and the final one is in Korea institute of energy research, Jeju global center, Korea [25,29,30]. To facilitate the scale-up and practical implementation of RED, more studies are required to make it more cost-effective and reliable.

As one of the steps toward this goal, this paper investigated the performance of the RED process under various operating conditions. Both theoretical and experimental approaches were taken to examine the effect of design and operating parameters such as cell pair, flow rate, temperature, and different salinity gradient on the power output performance of RED. The novelty of this work lies in a systematic analysis of RED performance based on the experimental works and the mathematical model, which will provide insight into the effective design and operation of RED processes.

2. Material, methods, and modeling

2.1. Lab-scale RED system

A lab-scale RED system was established to conduct experiments. Fig. 1a shows the schematic diagram of the RED system. The RED stack consisted of two endplates made of acrylic resin and 5–20 cell pairs in experiments. The RED stack was provided by Jeju Global Research Center, Korea Institute of Energy Research, and its details are presented in the literature [31]. Ion exchange membranes (IEMs) are stacked between the electrodes. The photography of the lab-scale RED system is presented in Fig. 1b.

The IEMs purchased from Fujifilm (Type-1, Fujifilm Manufacturing Europe, Netherlands) were used. The characteristics of these membranes are summarized in Table 1. The thicknesses of CEM and AEM were 125 and 124 μm, respectively. Their area resistances were 1.87 and 1.08 Ω cm^2, respectively. The transport numbers for the CEM and AEM were 0.952 and 0.963, respectively. The CEMs and AEMs are stacked sequentially and CEMs are located at the ends of cells pair as the shielding membranes.

Fig. 2 illustrates the cell pair of the stack. The membranes were separated from each other by a gasket and spacer. The gasket is made of polytetrafluoroethylene and has a thickness of 100 μm (Tommy Hecco, South Korea). The spacer is in the form of a mesh with 81.3% open area and a thickness of 100 μm (DS Mesh, South Korea) to prevent contact between membranes and to provide a channel for the feed solutions [32]. Between the shielding membrane (CEM) and the electrode, a different spacer (thickness 0.5 mm, Sefar, Korea) was used [33,34]. For electrode rinse solution, 50 mM of ferrocyanide and ferricyanide ($K_4Fe(CN)_6/K_3Fe(CN)_6$) solution was used. The effective membrane area is 0.0019 m^2 per cell.

The open circuit voltage (OCV) and power were measured by a source meter (Keithley 2401, SnM South Korea). Microflow pump (Lebanon, South Korea) were used to run the experiment at low flow conditions. The electrical conductivities of the high salinity and low salinity solutions passing through the RED stack were measured using a conductivity meter (WTW 3420, Germany).

2.2. Preparation of high salinity and low salinity solutions

The high salinity and low salinity solutions were prepared using deionized water and sodium chloride (NaCl). The NaCl (provided by Samchun South Korea) concentrations of the high salinity solutions (C_{HC}) were 0.6, 0.9, and 1.2 M. On the other hand, the NaCl concentration of the low salinity solutions (C_{LC}) was 5.0×10^{-5} M, 0.21, and 0.6 M, respectively. Each pair of the C_{HC} and C_{LC} simulates a scenario for the operation of RED systems. Table 2 summarizes the four pairs of the C_{HC} and C_{LC}.

2.3. Experimental conditions

The operating conditions for the RED experiments are also presented in Table 2. The cell pair, flow rate, concentration, and temperature were selected as the operational variables. The number of stacks was changed to 5, 10, 15, and 20, and the flow rates of the high salinity and low salinity solutions varied to 10, 20, 30, and 40 mL/min. In all experiments, the flow rate of the high salinity solution was set to be equal to that of the low salinity solution. The effect of the temperature was examined by varying it to 293, 313, and 333 K.

2.4. Model development

A simple model based on the Nernst's equations was developed to describe the phenomena occurring inside the cell in the RED system. The following considerations were taken into account: (1) continuously current flow distribution, (2) High salinity (HS) and low salinity (LS) streams are aqueous sodium chloride solution, and (3) the parameters required to obtain the OCV and gross power are evaluated under average conditions between the inlet and the outlet [35]. Eq. (1) shows the cell voltage equations which is evaluated through the Nernst equation.

$$\mathrm{Eocv}(i) = N_m \cdot \alpha_{\mathrm{CEM}} \cdot \frac{R \cdot T}{z \cdot F} \ln\left(\frac{\gamma_{\mathrm{HC}} \cdot C_{\mathrm{HC}}}{\gamma_{\mathrm{LC}} \cdot C_{\mathrm{LC}}}\right) + N_m \cdot \alpha_{\mathrm{AEM}} \cdot \frac{R \cdot T}{z \cdot F} \ln\left(\frac{\gamma_{\mathrm{HC}} \cdot C_{\mathrm{HC}}}{\gamma_{\mathrm{LC}} \cdot C_{\mathrm{LC}}}\right) \quad (1)$$

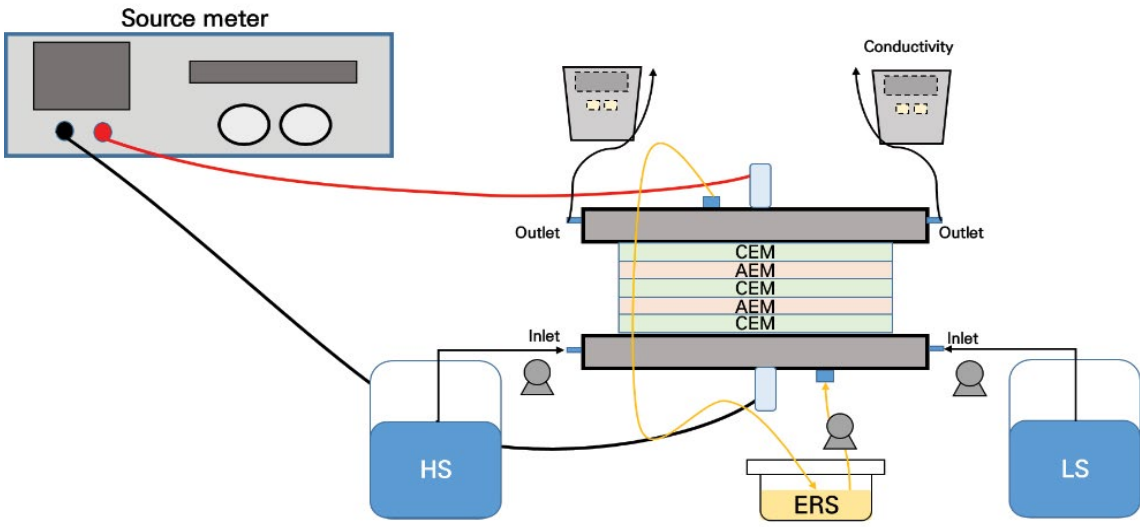

(a)

(b)

Fig. 1. (a) Schematic diagram of RED experimental equipment and (b) photography of the experimental setup.

where α_{CEM} and α_{AEM} are the permselectivity of cation and anion membranes respectively, F is Faraday's constant (96,485 C mol^{-1}), R is the Universal gas constant (8.31 J mol/K), T is the temperature (K), C is the ion concentration (mol m^{-3}), z is the valence and γ is the activity coefficient. This coefficient is determined by Debye–Hückel ($0 < C < 1$ M [36] or Pitzer ($C > 1$ M) equations [31]. The gross power, P, is calculated as the product of the output voltage and the electrical current, as shown in Eq. (2). The current was calculated by average current density on the cell length and the membrane area.

$$P = E \cdot I \tag{2}$$

The resistance of the red stack is the sum of the resistances for each cell in the stack. Internal losses in cell pairs are mainly divided into ohmic and non-ohmic resistors. Thus, R_i could be determined experimentally using the

Table 1
Characteristics of ion exchange membranes

Conditions		Specifications
Manufacture	CEM	Fujifilm (Type-1, Manufacturing
	AEM	Europe, Netherlands)
Thickness (μm)	CEM	125
	AEM	124
Area resistance (Ω cm^2)	CEM	1.87 ± 0.01
	AEM	1.08 ± 0.02
Transport number (–)	CEM	0.952
	AEM	0.963

electronic load. Vermaas et al. [37,38] explained this procedure in detail in previous works.

$$R_i(x) = R_{\text{ohmic}}(x) + R_{\text{non-ohmic}}(x) \tag{3}$$

Eq. (4) shows that the ohmic resistance. R_{ohmic} is determined by the membrane characteristics and compartment resistance of the HS and LS solutions.

$$R_{\text{ohmic}}(x) = N_m \cdot \left(\frac{R_{\text{CEM}}}{1-\beta} + \frac{R_{\text{AEM}}}{1-\beta} + \frac{h_{\text{HS}}}{\varepsilon^2 \cdot k_{\text{HS}}} + \frac{h_{\text{LS}}}{\varepsilon^2 \cdot k_{\text{LS}}} \right) \tag{4}$$

where R_{CEM} and R_{AEM} are the membrane resistances (Ω m^2), β is the mask factor of the membrane, ε is the porosity of the spacers (–), h_{HS}, and h_{LS} are intermembrane distances, and k_{HS} and k_{LS} are the electric conductivity of HS and LS solutions.

$$R_{\text{non-ohmic}}(x) = R_{\Delta c}(x) + R_{\text{BL}}(x) \tag{5}$$

where $R_{\Delta c}$ contributes to the resistance of the concentration change between the inlet and outlet. $R_{\Delta c}$ is calculated based on Eq. (5).

$$R_{\Delta c}(x) = N_m \cdot \alpha \cdot \frac{R \cdot T}{z \cdot F \cdot j \cdot \frac{A}{m^2}} \ln\left(\frac{A_{\text{LS}}(x)}{A_{\text{HS}}(x)} \right) \tag{6}$$

where $A_{\text{LS}}(x)$ and $A_{\text{HS}}(x)$ is area resistance due to bulk concentration.

$$R_{\text{BL}}(x) = N_m \cdot \left(\frac{0.62 t_{\text{res}} \cdot \frac{h_{\text{sea}}}{\text{LL}}}{\text{sec}} + 0.05 \right) \tag{7}$$

where t_{res} is resistance time inside the stack. t_{res} is calculated by Eq. (8).

$$t_{\text{res}} = \frac{L \cdot b \cdot \delta \cdot \in}{Q(x)} \tag{8}$$

where b is the width of the cell (m), L is the length of the cell (m). A MATLAB code was developed by combining the above equations, allowing the calculation of the OCV and power.

3. Results and discussions

3.1. Effect of the number of cell pairs

Fig. 3 shows the polarization curve of the RED system with a different number of cell pairs. The HS and LS solutions were the NaCl 35,000 mg/L solution and deionized water. The flow rates for the HS and LS solutions were set to 10 mL/min. As illustrated, the electrical potential decreases as an increase in the current, which is a typical pattern in RED systems. The OCV, which is the difference of electrical potential between two electrodes without any external load, was determined when the current was 0 A.

Table 3 summarizes the OCV values obtained from Fig. 3 at a different number of the cell pairs. It is evident from the results that the OCV is higher with a larger number

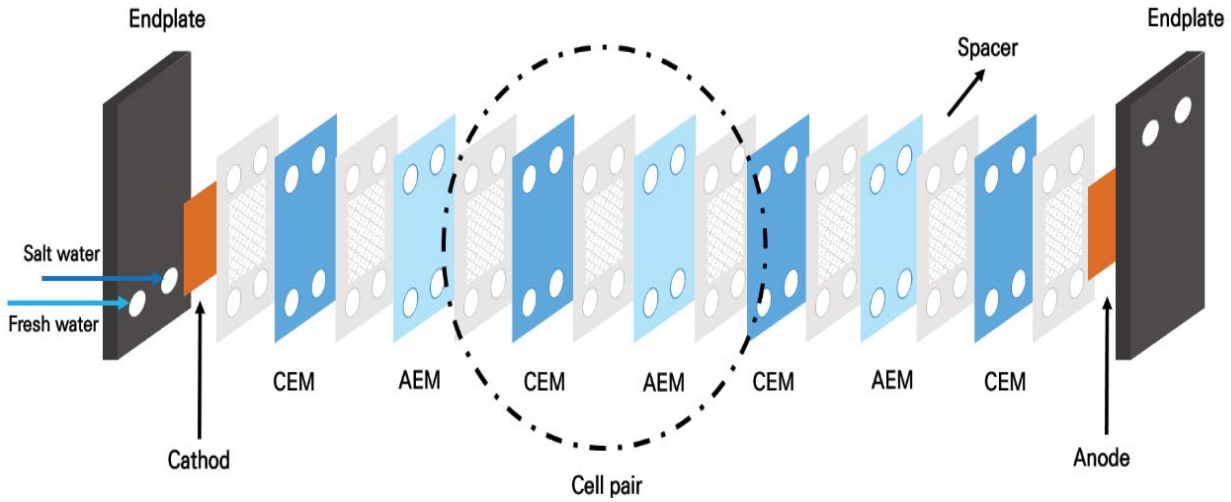

Fig. 2. Schematic diagram of the RED stack.

Table 2
Summary of experiment conditions

Conditions	Value
Cells pair (stack)	5, 10, 15, 20
Area of one membrane (m^2)	0.002
Q_{HC} (mL/min)	10, 20, 30, 40
Q_{LC} (mL/min)	10, 20, 30, 40
C_{HC}/C_{LC} (M)	0.6/0.00005 M (seawater/freshwater) 1.2/0.00005 M (brine/freshwater) 0.9/0.21 M (brine/brackish water) 1.2/0.6 M (brine/seawater)
Temperature (K)	293, 313, and 333

Table 3
Dependence of OCV on the number of cell pairs

Number of cells pairs	OCV (V)	OCV_{sim} (V)	Error (%)
5	0.8	0.8	0
10	1.47	1.58	7
15	2.17	2.18	1
20	2.75	3.5	21

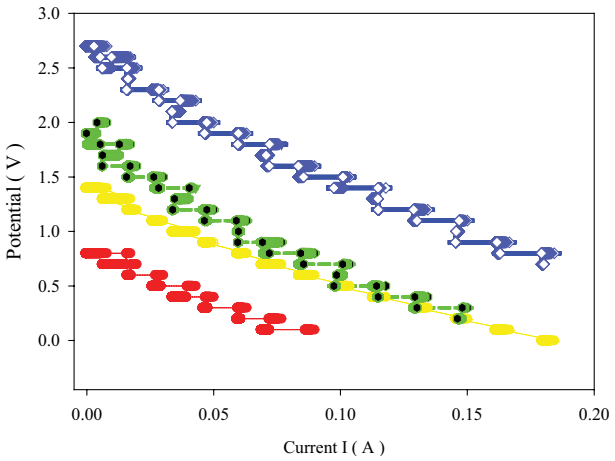

Fig. 3. Polarization curve of the RED system with a different number of cell pairs (red: 5 cells; yellow: 10 cells; green: 15 cells; blue: 20 cells).

of cell pairs. For example, the OCV was 0.8 with 5 cells and increased by 3.43 times with 20 cells. As the number of pairs increased, the OCV increased linearly. The experimental results were also compared with the model calculation (OVC_{sim}). When the number of the cell pairs was small, the model matched the experimental results well. As the number of the cell pairs increases, however, the error between the experimental results and the model calculations increases. This can be explained by the effect of concentration in the cell. In fact, the concentration increases at the outlet of the LS solution with an increase in the number of stacks. Since the model could not accurately reflect these phenomena, the deviations occur. Further calibration of the model may reduce them. Nevertheless, the current model can still reasonably describe the behaviors in OCV in the RED system.

In addition to the OCV, the gross power was also estimated from the power curves, which show the dependence of the power as a function of the current density. The experimental results and the model fits are shown in Fig. 4. The HS and LS solutions were also the NaCl 35,000 mg/L solution and deionized water. With an increase in the current density, the power increases and then decreases, resulting in the maximum power value in each case. For instance, the maximum power with the 5 cells is 0.02 W at the current density of 1.02 W/m^2. Overall, the maximum power increases as the number of cell pairs increases. The model fits were also carried out and the results are illustrated as solid curves in Fig. 5. Again, the model reasonably matches the experimental results. The deviations between the experiments and the model calculations also increase with an increase in the number of cell pairs. This can be explained by the concentration effect that was previously mentioned.

Table 4 summarizes the dependence of the maximum power on the number of cell pairs. The maximum power density changes from 0.02 to 0.11 with an increase in the number of cell pairs from 5 cells to 20 cells. The model estimated the maximum power well and the error ranges from 5.1% to 9.1%. It appears that the model accuracy was slightly higher for the estimation of the maximum power density than for the OCV. This suggests that the concentration effect is less influential on the maximum power density than on the OCV.

3.2. Effect of flow rate

Fig. 5a shows the dependence of OCV on the flow rates of the HS and LS solutions in the RED system with 10 cells. The symbols indicate the experimental data while the solid curve represents the model results. As illustrated, the OCV increases with an increase in the flow rate of up to 40 mL/min. But a further increase in the flow rate does not result in an increased OCV. In general, an increase in the feed flow rates leads to higher OCV because the residence time for ion exchange is lower keeping a higher salinity gradient along with the cell [33]. However, the OCV cannot be proportional to the flow rate since the number of cell pairs is a limiting factor. When the number of cell pairs is 20, the OCV increases with the flow rate up to 60 mL/min, as shown in Fig. 5b. This implies that the optimum flow rate to have high OCV exists depending on the system.

The model calculations were compared with the experimental results in Table 5. The model can properly show the effect of the flow rate on the OCV. Again, the errors of the model calculation are slightly higher at a low flow rate. But the differences between the model and experimental results decrease as the flow rate increases. This is attributed to the reduction in the salt concentration at the end of the stack by the increased flow rate. This suggests that the accuracy of the model calculation increases with an increase in the flow rate.

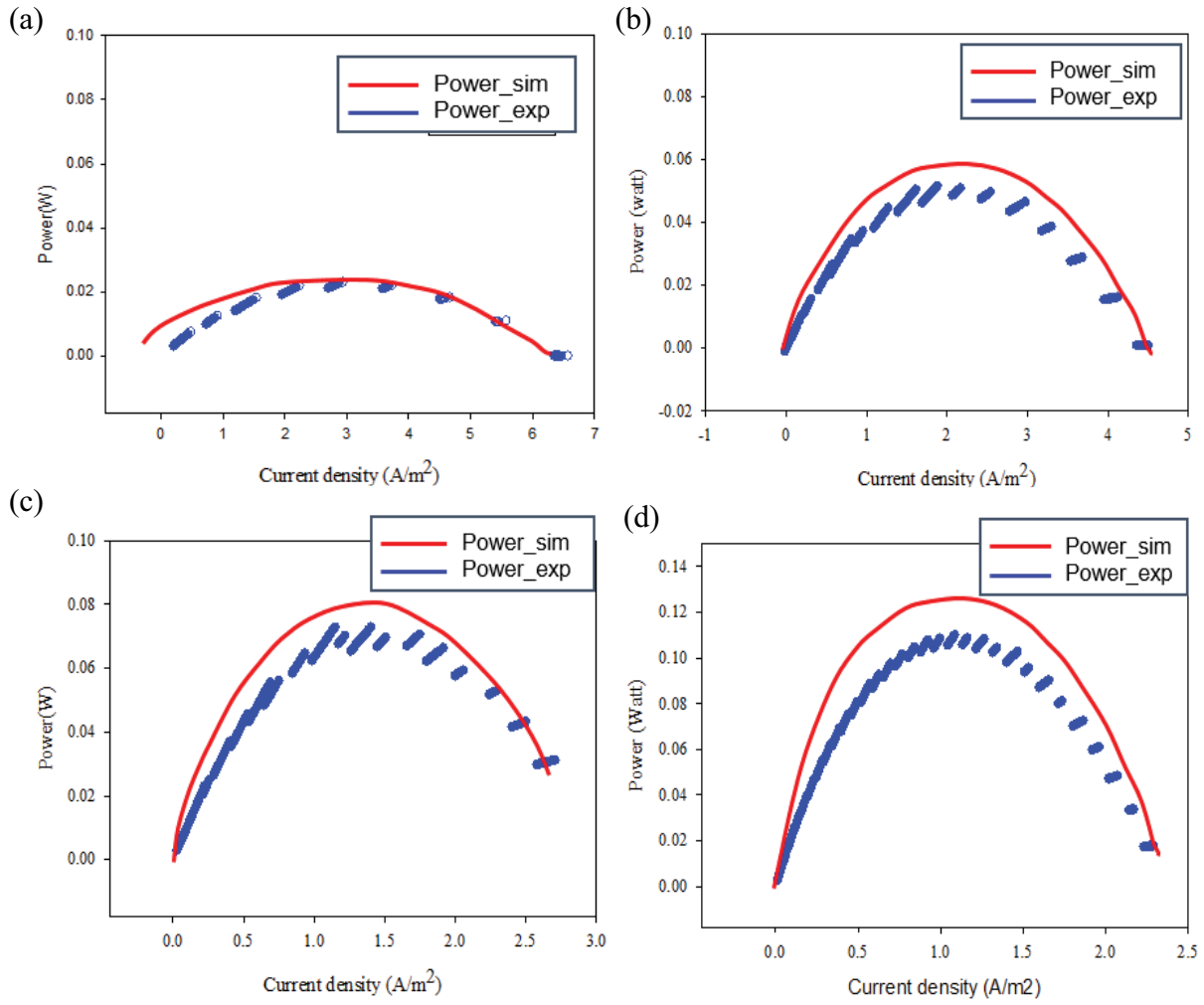

Fig. 4. Dependence of power on current density in a different number of the cell pairs (symbol: experimental data; solid curve: model calculations) (a) 5 cells, (b) 10 cells, (c) 15 cells, and (d) 20 cells.

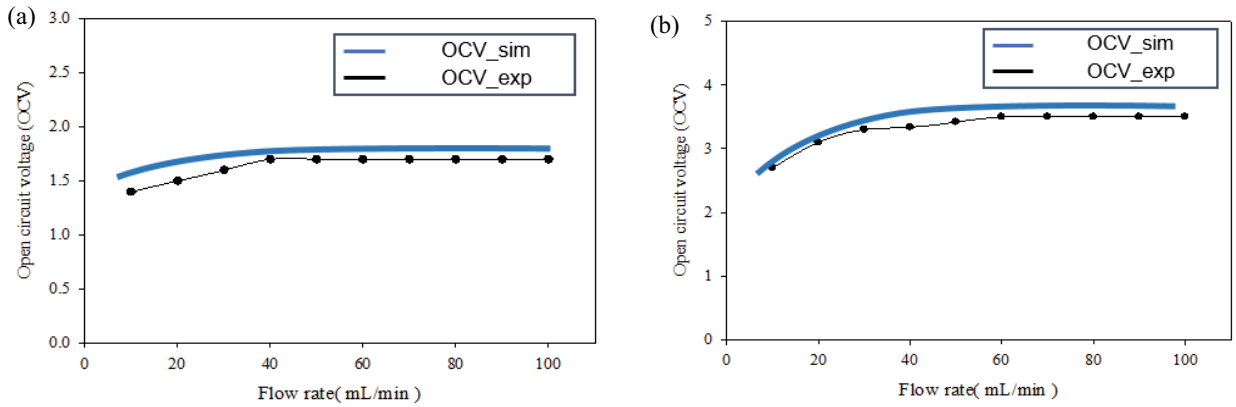

Fig. 5. Dependence of OCV on flow rate (symbol: experimental data; solid curve: model calculations) (a) 10 cells and (b) 20 cells.

The flow rate may also affect the power generation in RED as well as the OCV. Table 6 compares the power curves at different flow rates in the RED system. With the number of cell pairs of 10, the power generation does not seem to increase by increasing the flow rate. Instead, the pressure drop inside the stack increases with the flow rate. This suggests that the net energy generated by the RED system may be lower at a higher flow rate. With the use of 20 cells, the

Table 4
Dependence of power on the number of cell pairs

Number of cells pairs	Power (W)	$Power_{sim}$ (W)	Flow rate	Temperature	High salinity solution	Low salinity solution
5	0.02 (1.02 W/m^2)	0.02 (1.02 W/m^2)	10 mL/min	293 K	35,000 ppm (NaCl)	DI water
10	0.05 (1.27 W/m^2)	0.053 (1.35 W/m^2)	10 mL/min			
15	0.078 (1.32 W/m^2)	0.082 (1.39 W/m^2)	10 mL/min			
20	0.11 (1.4 W/m^2)	0.12 (1.52 W/m^2)	10 mL/min			

Table 5
Effect of flow rate on OCV for RED systems with 10 and 20 cells

Flow rate	OCV_{exp} (V)	OCV_{sim} (V)	Error (%)	OCV_{exp} (V)	OCV_{sim} (V)	Error (%)
	10 cells			20 cells		
10 mL/min	1.4	1.58	12.9	2.7	3.5	29.6
20 mL/min	1.5	1.63	8.7	3.0	3.5	16.7
30 mL/min	1.6	1.68	5.0	3.1	3.5	12.9
40 mL/min	1.7	1.72	1.2	3.2	3.5	9.4
50 mL/min	1.7	1.75	2.9	3.3	3.5	6.1
60 mL/min	1.7	1.75	2.9	3.4	3.5	2.9
70 mL/min	1.7	1.75	2.9	3.4	3.5	2.9
80 mL/min	1.7	1.75	2.9	3.4	3.5	2.9
90 mL/min	1.7	1.75	2.9	3.4	3.5	2.9
100 mL/min	1.7	1.75	2.9	3.4	3.5	2.9

Table 6
Effect of flow rate on P_{max} for RED systems with 10 and 20 cells

Number of cell pairs	Flow rate	P_{max} (W)	Pressure drop (bar)	Temperature	HS solution	LS solution
10 cells	10 mL/min	0.051	0.7	293 K	35,000 ppm (NaCl)	3 ppm (DI water)
	20 mL/min	0.057	1.35			
	30 mL/min	0.054	2.1			
	40 mL/min	0.049	2.8			
20 cells	10 mL/min	0.08	0.3			
	20 mL/min	0.11	0.61			
	30 mL/min	0.12	0.94			
	40 mL/min	0.12	1.16			

power slightly increases with the flow rate but the pressure drop also increases. Again, it appears that an increase in the flow rate over 20 mL/min is effective to increase the power generation even with the use of 20 cells. It should be noted that there is an optimum flow rate depending on the number of cell pairs.

As a result of the flow rate, the P_{max} was less sensitive to the flow rate. With 10 cells, the P_{max} was not affected by the flow rate. With 20 cells, however, the P_{max} slightly increased with the flow rate. Nevertheless, the pressure drop inside the channel in the RED stack increased with an increased flow rate, suggesting that the flow rate should be optimized by considering the number of the cell pairs and the pressure drop.

3.3. Effect of temperature

The current dependent variations in voltage and power are shown in Fig. 6 for several temperatures including 293, 313, and 333 K. The temperature increases both the voltage and power. With an increase in the temperature from 293 to 313 K, the power goes up by 12%. A further increase of up to 333 K results in the power increase by 16%. The OCV was determined from the voltage curve. The OCV

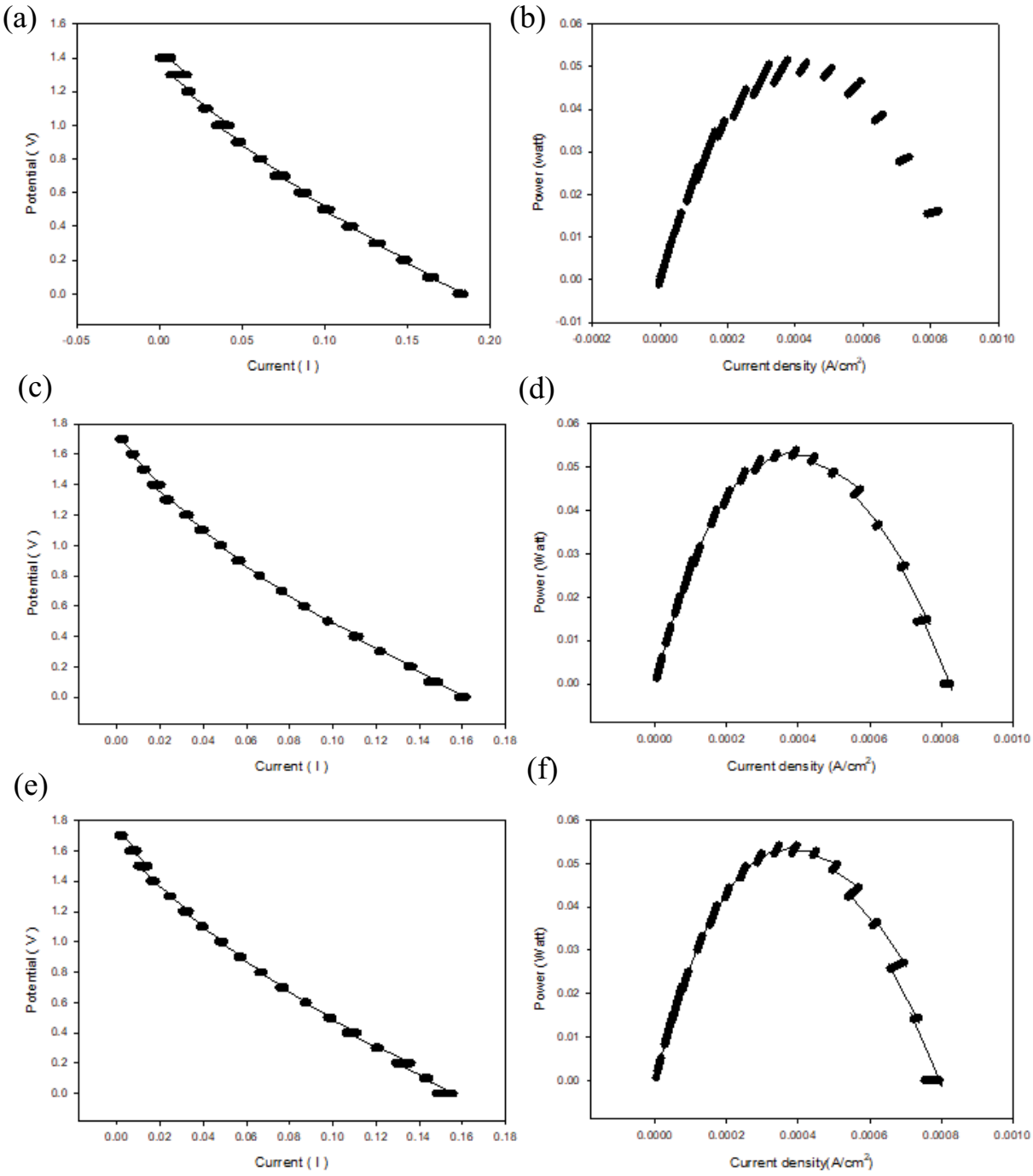

Fig. 6. Polarization and power curves at different temperatures (a) polarization curve at 293 K, (b) power curve at 293 K, (c) polarization curve at 313 K, (d) power curve at 313 K, (e) polarization curve at 333 K, and (f) power curve at 333 K.

values were 1.4 V at 293 K, 1.6 V at 313 K, and 1.8 V at 333 K, respectively. This is attributed to a decrease in membrane resistance by increasing temperature [39]. Previous works [23,33] also report a significant increase in the RED performance as the temperature increased from 283 to 293 K. In Table 7, the model calculations for the OCV and power at different temperatures were compared with the experimental results. The model matches the OCV and power well. The temperature increases both the voltage and power, which is attributed to a decrease in membrane resistance by increasing the temperature [40].

3.4. Effect of concentration

Depending on the types of the application, the HS and LS solutions for RED systems are different. For instance,

seawater may be used as the HS solution and freshwater such as river water or reclaimed wastewater may be used as the LS solution. If RES is used in a desalination plant, brine from the SWRO process is used as the HS solution and other low salinity water sources are used as the LS solution. In this study, four scenarios are considered: seawater (HS)/fresh water (LS), brine (HS)/fresh water (LS); brine (HS)/brackish water (LS); and brine (HS)/seawater (LS). In each case, the salt concentrations for the HS and LS solutions were adjusted to simulate the scenario. As shown in Fig. 7, the RED experiment was performed at 293 K with a flow rate of 10 mL/min. The results are summarized in Table 8. As expected, the OCV and P_{max} were higher at a higher salinity difference between the HS and LS solutions. The highest OCV and P_{max} were obtained in the scenario of brine (HS)/fresh water (LS). On the other hand, only negligible OCV and P_{max} were observed in the scenarios of brine (HS)/brackish water (LS); and brine (HS)/seawater (LS). The model results in good agreement with the experimental data with the errors ranging from 0% to 18%.

It should be noted that both the salinity gradient and the salt concentrations are important factors affecting the power

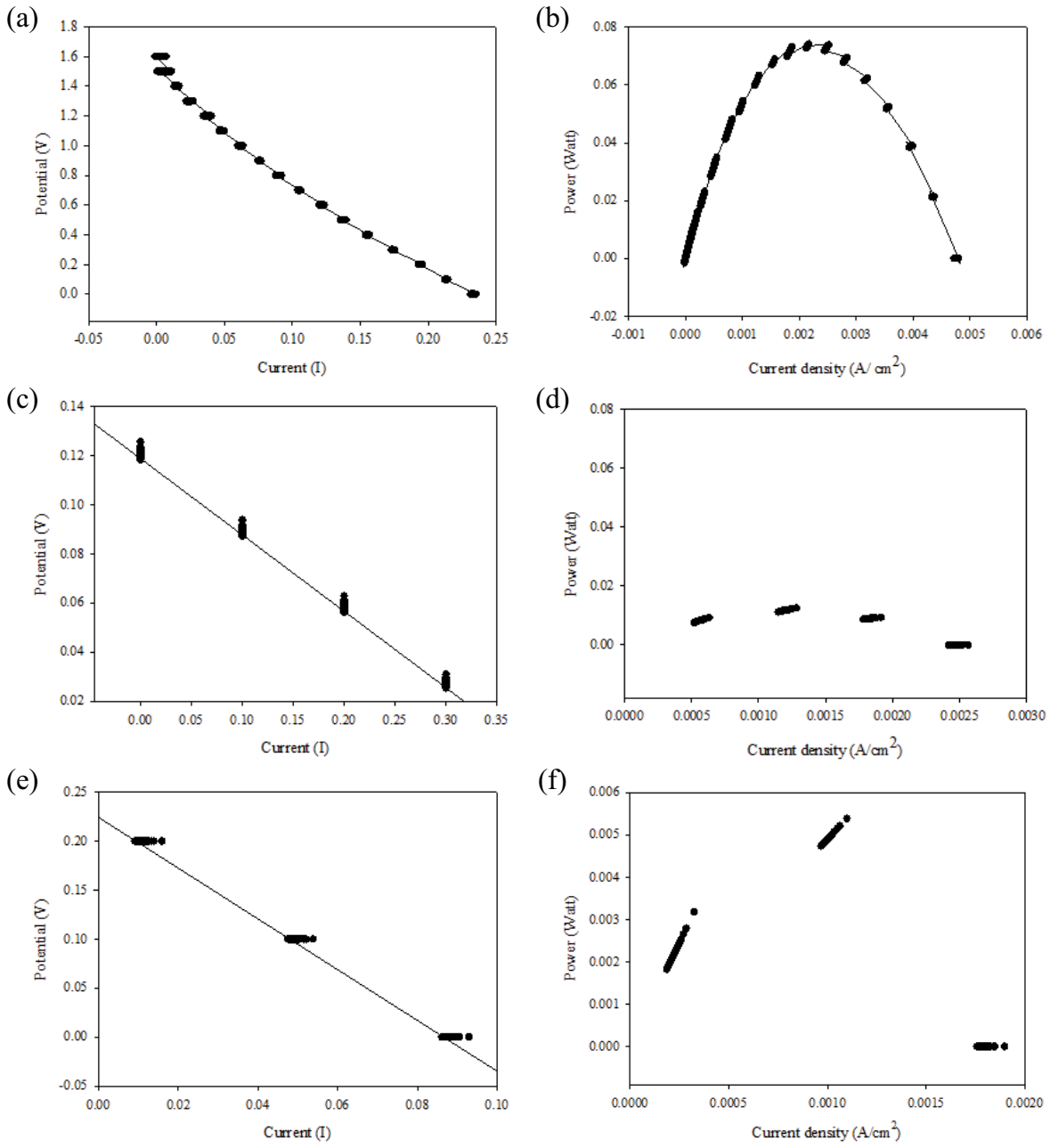

Fig. 7. Polarization and power curves at different concentrations. (a and b) Polarization and power curves (HSS: 70,000 mg/L, LSS: 50 mg/L), (c and d) polarization and power curves (HSS: 52,500 mg/L, LSS: 12,500 mg/L), (e and f) polarization and power curves (HSS: 70,000 mg/L, LSS: 35,000 mg/L).

Table 7
Effect of temperature on OCV and P_{max}

Temperature	Number of cell pairs	OCV_{exp}	OCV_{sim}	Error (%)	P_{max_exp} (W)	P_{max_sim} (W)
293 K	10	1.4	1.58	11	0.05 (1.3 W/m^2)	0.059 (1.5 W/m^2)
313 K	10	1.6	1.6	0	0.056 (1.36 W/m^2)	0.07 (1.7 W/m^2)
333 K	10	1.8	1.8	0	0.058 (1.47 W/m^2)	0.08 (2.1 W/m^2)

Table 8
Effect of concentrations for HS and LS solutions on OCV and P_{max}

Scenario	Concentration (ppm)	OCV_{exp} (V)	OCV_{sim} (V)	P_{max} (W)	Error (%)
Seawater/freshwater	HS: 35,000 LS: 50	1.4	1.58	0.05	10%
Brine/freshwater	HS: 70,000 LS: 50	1.6	1.9	0.075	18%
Brine/brackish water	HS: 52,500 LS: 12,500	0.1	0.1	0.01	0%
Brine/Seawater	HS: 70,000 LS: 35,000	0.2	0.1	0.01	0%

generation by the RED system. In the scenarios of seawater (HS)/freshwater (LS) and brine (HS)/seawater (LS), the net salinity difference is 35,000 mg/L. Nevertheless, the P_{max} for seawater (HS)/freshwater (LS) is much higher than that for brine (HS)/seawater (LS). This is because the voltage loss due to ion exchange between HS and LS solutions increases with an increase in the concentration. In addition, the permselectivity of ion exchange membranes is reduced by an increase in the concentration. Similar results were reported in the literature [36]. As a result, the OCV and P_{max} were higher at a higher salinity difference between the HS and LS solutions. Nevertheless, the OCV and P_{max} were smaller at a higher salt concentration even if the salinity gradient between the HS and LS solutions were the same.

4. Conclusions

In this study, the effect of operating conditions on the performance of a RED system was theoretically and experimentally investigated. It was found that the OCV and P_{max} were higher with a larger number of cell pairs. The OCV increased with an increase in the flow rate up to a certain value but a further increase in the flow rate was not effective. On the power hand, the P_{max} was less sensitive to the flow rate. An increase in the temperature and salinity gradient results in increased OCV and P_{max}. The model reasonably matched the experimental results. Based on these findings, it is recommended to increase the number of the cell pairs and salinity gradient to achieve high performance in the RED system. Nevertheless, the optimum flow rate should be determined by considering its effectiveness on the RED performance.

Acknowledgments

This research was supported by National Research of Korea (NRF-2017M1A2A2047551).

References

[1] Z. Zhou, M. Benbouzid, J. Frédéric Charpentier, F. Scuiller, T. Tang, A review of energy storage technologies for marine current energy systems, Renewable Sustainable Energy Rev., 18 (2013) 390–400.
[2] B.E. Logan, M. Elimelech, Membrane-based processes for sustainable power generation using water, Nature, 488 (2012) 313–319.
[3] Z. Jia, B. Wang, S. Song, Y. Fan, Blue energy: current technologies for sustainable power generation from water salinity gradient, Renewable Sustainable Energy Rev., 31 (2014) 91–100.
[4] F. Helfer, C. Lemckert, The power of salinity gradients: an Australian example, Renewable Sustainable Energy Rev., 50 (2015) 1–16.
[5] Z. Jalili, K.W. Krakhella, K.E. Einarsrud, O.S. Burheim, Energy generation and storage by salinity gradient power: a model-based assessment, J. Energy Storage, 24 (2019) 100755.
[6] C. Seyfried, H. Palko, L. Dubbs, Potential local environmental impacts of salinity gradient energy: a review, Renewable Sustainable Energy Rev., 102 (2019) 111–120.
[7] N.Y. Yip, M. Elimelech, Thermodynamic and energy efficiency analysis of power generation from natural salinity gradients by pressure retarded osmosis, Environ. Sci. Technol., 46 (2012) 5230–5239.
[8] R.A. Tufa, E. Curcio, W. van Baak, J. Veerman, S. Grasman, E. Fontananova, G. Di Profio, Potential of brackish water and brine for energy generation by salinity gradient power-reverse electrodialysis (SGP-RE), RSC Adv., 4 (2014) 42617–42623.
[9] Y. Chen, A.A. Alanezi, J. Zhou, A. Altaee, M.H. Shaheed, Optimization of module pressure retarded osmosis membrane

for maximum energy extraction, J. Water Process Eng., 32 (2019) 100935.
[10] A. Altaee, A. Cippolina, Modeling, and optimization of a modular system for power generation from a salinity gradient, Renewable Energy, 141 (2019) 139–147.
[11] S. Lee, J. Choi, Y.-G. Park, H. Shon, C.H. Ahn, S.-H. Kim, Hybrid desalination processes for beneficial use of reverse osmosis brine: current status and future prospects, Desalination, 454 (2019) 104–111.
[12] M. Tedesco, A. Cipollina, A. Tamburini, G. Micale, Towards 1 kW power production in a reverse electrodialysis pilot plant with saline waters and concentrated brines, J. Membr. Sci., 522 (2017) 226–236.
[13] J. Veerman, M. Saakes, S.J. Metz, G.J. Harmsen, Electrical power from sea and river water by reverse electrodialysis: a first step from the laboratory to a real power plant, Environ. Sci. Technol., 44 (2010) 9207–9212.
[14] J. Veerman, M. Saakes, S. Metz, G. Harmsen, Reverse electrodialysis: performance of a stack with 50 cells on the mixing of sea and river water, J. Membr. Sci., 327 (2009) 136–144.
[15] R. Pattle, Production of electric power by mixing fresh and saltwater in the hydroelectric pile, Nature, 174 (1954) 660–660.
[16] G. Wick, Prospects for renewable energy from sea, Mar. Technol. Soc. J., 11 (1977) 16–21.
[17] J.N. Weinstein, F.B. Leitz, Electric power from differences in salinity: the dialytic battery, Science, 191 (1976) 557–559.
[18] E. Fontananova, D. Messana, R. Tufa, I. Nicotera, V. Kosma, E. Curcio, W. van Baak, E. Drioli, G. Di Profio, Effect of solution concentration and composition on the electrochemical properties of ion exchange membranes for energy conversion, J. Power Sources, 340 (2017) 282–293.
[19] M. Tedesco, C. Scalici, D. Vaccari, A. Cipollina, A. Tamburini, G. Micale, Performance of the first reverse electrodialysis pilot plant for power production from saline waters and concentrated brines, J. Membr. Sci., 500 (2016) 33–45.
[20] J. Veerman, M. Saakes, S.J. Metz, G. Harmsen, Reverse electrodialysis: evaluation of suitable electrode systems, J. Appl. Electrochem., 40 (2010) 1461–1474.
[21] J. Veerman, J. Post, M. Saakes, S. Metz, G. Harmsen, Reducing power losses caused by ionic shortcut currents in reverse electrodialysis stacks by a validated model, J. Membr. Sci., 310 (2008) 418–430.
[22] J.G. Hong, T.-W. Park, Y. Dhadake, Property evaluation of custom-made ion exchange membranes for electrochemical performance in reverse electrodialysis application, J. Electroanal. Chem., 850 (2019) 113437.
[23] J. Veerman, M. Saakes, S. Metz, G. Harmsen, Reverse electrodialysis: a validated process model for design and optimization, Chem. Eng. J., 166 (2011) 256–268.
[24] L. Gurreri, G. Battaglia, A. Tamburini, A. Cipollina, G. Micale, M. Ciofalo, Multi-physical modeling of reverse electrodialysis, Desalination, 423 (2017) 52–64.
[25] M. Tedesco, E. Brauns, A. Cipollina, G. Micale, P. Modica, G. Russo, J. Helsen, Reverse electrodialysis with saline waters and concentrated brines: a laboratory investigation towards technology scale-up, J. Membr. Sci., 492 (2015) 9–20.
[26] Y. Mei, C.Y. Tang, Recent developments and future perspectives of reverse electrodialysis technology: a review, Desalination, 425 (2018) 156–174.
[27] D.A. Vermaas, M. Saakes, K. Nijmeijer, Doubled power density from salinity gradients at reduced intermembrane distance, Environ. Sci. Technol., 45 (2011) 7089–7095.
[28] J.G. Hong, W. Zhang, J. Luo, Y. Chen, Modeling of power generation from the mixing of simulated saline and freshwater with a reverse electrodialysis system: the effect of monovalent and multivalent ions, Appl. Energy, 110 (2013) 244–251.
[29] M. Tedesco, H. Hamelers, P. Biesheuvel, Nernst–Planck transport theory for (reverse) electrodialysis: I. effect of co-ion transport through the membranes, J. Membr. Sci., 510 (2016) 370–381.
[30] P. Długołęcki, J. Dąbrowska, K. Nijmeijer, M. Wessling, Ion conductive spacers for increased power generation in reverse electrodialysis, J. Membr. Sci., 347 (2010) 101–107.
[31] J.-Y. Nam, K.-S. Hwang, H.-C. Kim, H. Jeong, H. Kim, E. Jwa, S. Yang, J. Choi, C.-S. Kim, J.-H. Han, Assessing the behavior of the feed-water constituents of a pilot-scale 1,000-cell-pair reverse electrodialysis with seawater and municipal wastewater effluent, Water Res., 148 (2019) 261–271.
[32] A. D'Angelo, M. Tedesco, A. Cipollina, A. Galia, G. Micale, O. Scialdone, Reverse electrodialysis performed at pilot plant scale: evaluation of redox processes and simultaneous generation of electric energy and treatment of wastewater, Water Res., 125 (2017) 123–131.
[33] R. Ortiz-Imedio, L. Gomez-Coma, M. Fallanza, A. Ortiz, R. Ibañez, I. Ortiz, Comparative performance of salinity gradient power-reverse electrodialysis under different operating conditions, Desalination, 457 (2019) 8–21.
[34] R.A. Tufa, E. Curcio, E. Brauns, W. van Baak, E. Fontananova, G. Di Profio, Membrane distillation and reverse electrodialysis for near-zero liquid discharge and low energy seawater desalination, J. Membr. Sci., 496 (2015) 325–333.
[35] P. Długołęcki, A. Gambier, K. Nijmeijer, M. Wessling, Practical potential of reverse electrodialysis as process for sustainable energy generation, Environ. Sci. Technol., 43 (2009) 6888–6894.
[36] M. Tedesco, A. Cipollina, A. Tamburini, I.D.L. Bogle, G. Micale, A simulation tool for analysis and design of reverse electrodialysis using concentrated brines, Chem. Eng. Res. Des., 93 (2015) 441–456.
[37] D.A. Vermaas, E. Guler, M. Saakes, K. Nijmeijer, Theoretical power density from salinity gradients using reverse electrodialysis, Energy Procedia, 20 (2012) 170–184.
[38] D.A. Vermaas, M. Saakes, K. Nijmeijer, Power generation using profiled membranes in reverse electrodialysis, J. Membr. Sci., 385–386 (2011) 234–242.
[39] S. Yang, W.-S. Kim, J. Choi, Y.-W. Choi, N. Jeong, H. Kim, J.-Y. Nam, H. Jeong, Y.H. Kim, Fabrication of photocured anion-exchange membranes using water-soluble siloxane resins as cross-linking agents and their application in reverse electrodialysis, J. Membr. Sci., 573 (2019) 544–553.
[40] F. Giacalone, F. Vassallo, L. Griffin, M. Ferrari, G. Micale, F. Scargiali, A. Tamburini, A. Cipollina, Thermolytic reverse electrodialysis heat engine: model development, integration and performance analysis, Energy Convers. Manage., 189 (2019) 1–13.